Eur. Phys. J. D (2006)
DOI: 10.1140/epjd/e2006-00201-5

THE EUROPEAN PHYSICAL JOURNAL D

Competing processes for electron capture to continuum in relativistic ion-atom collisions

D.H. Jakubaßa-Amundsen[a]

Mathematics Institute, University of Munich, Theresienstrasse 39, 80333 Munich, Germany

Received 6 April 2006 / Received in final form 3 July 2006
Published online 6 September 2006 –

Abstract. The relative importance of the two mechanisms for the capture of a target electron by a fast, heavy projectile, radiative ionization (RI) and Coulomb capture to continuum (ECC), is studied in the vicinity of the forward peak. For both processes a consistent relativistic description, based on the impulse approximation, is provided. It is found that the differential cross-sections scale with the projectile charge and exhibit a common velocity dependence. As a result, RI starts to dominate over ECC near the same impact energy (∼11 MeV/amu) for arbitrary bare projectiles colliding with hydrogen. For electrons from the inner shells of heavier targets this energy increases, however, which is confirmed by a coincidence experiment on 90 MeV/amu U^{88+} + N_2.

PACS. 34.70.+e Charge transfer – 41.60.-m Radiation by moving charges

1 Introduction

The interest in the field of electron and photon emission in relativistic heavy ion-atom collisions has been revived by the feasibility of measuring multiparticle momentum distributions in coincidence, made possible by the COLTRIMS detector technique [1]. At the ESR storage ring of GSI in Darmstadt, Germany, first measurements of the spectrum of cusp electrons from collisions with fast, highly stripped uranium projectiles have been reported by Hagmann and collaborators [2,3]. In these experiments, the forward electrons are measured in coincidence either with the emitted photons or with the charge state of the transmitted projectiles.

This feasibility of simultaneously measuring radiative and nonradiative electron capture to continuum in relativistic ion-atom collisions calls for a theoretical reinvestigation of the question at which collision velocity v the simultaneous emission of an electron, which has slowed down to near-zero energy in the projectile frame of reference, and a 'bremsstrahlung' photon which carries away the excess energy (the RI process), starts to dominate over the 'no-photon' electron capture to continuum (ECC) process. The relevance of this so-called crossing velocity is threefold. Firstly, ECC rapidly drops with velocity due to the increasing momentum transfer which is required for this process, such that for projectiles carrying electrons (e.g. U^{88+}) it is understood that in energetic collisions, the cusp electrons predominantly result from electron loss. However, at sufficiently high velocities when RI comes into play with its considerably slower decrease with v, electron capture (via RI) may again compete with electron loss. Secondly, the cusp shape is a subtle indicator of the strength and action of the perturber field. For bare projectiles, this shape changes near the crossing velocity. Whereas for ECC the cusp is skewed to the low-energy side, electrons from RI are emitted with much larger intensity at the high-energy side. Thirdly, if at a given collision energy RI provides much larger cross-sections than ECC, RI may (for bare projectiles) be identified even in a singles experiment. It is shown below that the crossing velocity of the two processes is by no means unique but depends — in an easily predictable way — on the collision system.

Early investigations of this crossing velocity date back to the work of Briggs and Dettmann [4] for capture to bound states and, by invoking continuity across the ionization threshold, to Rudd and Macek [5], Shakeshaft and Spruch [6] and Lucas et al. [7] for capture to continuum. Within a large-v expansion of the nonrelativistic first-order Born formalism, they found a common crossing velocity $v_{cr} \sim 23$ a.u. (13 MeV/amu collision energy) for all bare projectiles (of nuclear charge Z_P) colliding with hydrogen. This Z_P-independence of v_{cr} was related to a common scaling of RI and ECC with Z_P^3.

The crossing velocity was also studied for helium targets. Using the same approach as [6], Martiarena and Garibotti [8] obtained a lower value for v_{cr} (∼20.5 a.u.). This result was later contradicted by calculations within

[a] e-mail: doris.jaku@lrz.uni-muenchen.de

a higher-order theory, providing a crossing velocity $v_{cr} \sim 30$ a.u. for carbon and neon colliding with He [9].

The aim of the present work is to investigate possible common scaling properties of the two processes as well as the determination of the crossing velocity within a higher-order relativistic theory which is required for a correct description of the capture processes. We will apply the impulse approximation (IA) which is particularly suited for asymmetric collision systems. In the case of electron capture by heavy projectiles, the loosely bound target electrons are in this model viewed as quasifree particles which scatter inelastically from the projectile. For radiative capture to continuum in energetic collisions, the impulse approximation is a well-established theory [10,11]. Recently, a relativistic formulation of the IA was provided [12] and tested against experimental photon spectra from 220 MeV/amu U^{90+} + N_2 collisions near the short-wavelength limit [13,14]. The impulse approximation has also been successful in describing the cusp electrons from the radiationless capture process in nonrelativistic collision systems, concerning the cusp asymmetry [15,16] as well as the peak intensity [17].

The paper is organized as follows. The theory part, Section 2, provides a relativistic formulation of ECC as well as the essential formulae for radiative ionization. Electron spectra in the forward direction for RI and ECC and the relative importance of both processes are discussed in Section 3 for the two collision systems 30 MeV/amu Ar^{18+} + H and 200 MeV/amu U^{92+} + H. The peak values of the doubly differential cross-sections at the cusp in nucleus-hydrogen collisions are used to extract the velocity- and projectile charge-dependence as well as the RI/ECC crossing velocity. The behaviour for heavier targets is also addressed. Concluding remarks are given in Section 4. Atomic units ($\hbar = m = e = 1$) are used unless otherwise indicated.

2 Relativistic theory

We consider the ionization of a light target by a fast and heavy, bare projectile. The process where the electrons are emitted into low-lying energy states relative to the projectile, is described by means of electron capture to continuum. Within the single-particle approximation, the general expression for the transition amplitude from an initially bound target state to a projectile continuum state $\overline{\psi_{f,P}^{(\sigma_f)'}(x')} = \psi_{f,P}^{(\sigma_f)'+}(x')\gamma_0$ of momentum $\boldsymbol{k}'_f$ and spin σ_f is given by

$$a_{fi} = -\frac{i}{c}\int d^4x' \overline{\psi_{f,P}^{(\sigma_f)'}(x')} d_\lambda^+ \left(\hat{S}\mathbb{A}(x)\hat{S}^{-1}\right)\hat{S}\Psi_i^{(\sigma_i)}(x). \tag{2.1}$$

The RI and ECC processes differ only in the choice of the electromagnetic transition field $\mathbb{A}(x)$ and in the presence (RI) or absence (ECC) of the photon creation operator d_λ^+ in (2.1). Projectile-frame related quantities are denoted by a prime, and we have chosen this frame as our frame of reference. $\Psi_i^{(\sigma_i)}(x)$ is the exact scattering state which relates asymptotically to a target eigenstate $\psi_{i,T}^{(\sigma_i)}(x)$ with spin σ_i and space-time vector $x = (ct, \boldsymbol{x})$. x' is connected to x by a Lorentz transformation. The target state has to be transformed into the projectile frame by means of the Lorentz boost operator $\hat{S}$. If the z-axis (respectively the unit vector $\boldsymbol{e}_z$) is chosen along the collision velocity $\boldsymbol{v}$, then

$$\hat{S}(v) = \sqrt{\frac{1+\gamma}{2}}\left(1 - \frac{\gamma v/c}{1+\gamma}\alpha_z\right) \tag{2.2}$$

with its inverse $\hat{S}^{-1}(v) = \gamma_0\hat{S}(v)\gamma_0 = \hat{S}(-v)$. α_z, γ_0 are Dirac matrices [18] and $\gamma = (1 - v^2/c^2)^{-\frac{1}{2}}$.

2.1 Nonradiative capture (ECC)

The derivation of the relativistic impulse approximation for ECC proceeds in the same way as in the case of radiative ionization [12]. For radiationless transitions, the interaction $\mathbb{A}(x)$ results from the target Coulomb potential V_T. Transformed into the projectile reference frame, one has

$$\begin{aligned}\gamma_0\hat{S}\mathbb{A}(x)\hat{S}^{-1} &= \gamma_0\hat{S}\gamma_0 V_T(\boldsymbol{x})\hat{S}^{-1} \\ &= \gamma V_T(\boldsymbol{x})\left(1 + \frac{v}{c}\alpha_z\right).\end{aligned} \tag{2.3}$$

For weak target potentials ($Z_T \ll Z_P$ with Z_T the target nuclear charge) or high collision velocities ($v \gg Z_T/n_i$ with n_i the initial-state main quantum number), we may assume that the active electron propagates exclusively in the projectile field, and we may also neglect off-shell effects. This leads to the impulse approximation where the scattering state is approximated by

$$\hat{S}\Psi_i^{(\sigma_i)}(x) = \frac{1}{c}\sum_{s=1}^{4}\int d\boldsymbol{q}\, d\omega_q \psi_{q,P}^{(s)'}(x')\left(q_s'(x'), \hat{S}\psi_{i,T}^{(\sigma_i)}(x)\right). \tag{2.4}$$

Here, the electron's intermediate state $\psi_{q,P}^{(s)'}(x')$ is a projectile continuum eigenstate with momentum $\boldsymbol{q}$ and energy $\delta_s\omega_q$, and $q_s'(x')$ is a relativistic plane wave characterized by the four-spinor $u_q^{(s)}$ [19]. $s = 1, 2$ denotes the spin directions $+, -$ for the particle states (with $\delta_s = +1$), and $s = 3, 4$ correspond to the antiparticle states ($\delta_s = -1$).

Let E_i^T and E_f' be the initial and final electronic energies, respectively. We separate the time-dependence,

$$\begin{aligned}&\psi_{i,T}^{(\sigma_i)}(x) = e^{-iE_i^T t}\psi_{i,T}^{(\sigma_i)}(\boldsymbol{x}),\ \ \psi_{f,P}^{(\sigma_f)'}(x') = e^{-iE_f' t'}\psi_{f,P}^{(\sigma_f)'}(\boldsymbol{x}'), \\ &\psi_{q,P}^{(s)'}(x') = (2\pi)^{-\frac{1}{2}}e^{-i\delta_s\omega_q t'}\psi_{q,P}^{(s)'}(\boldsymbol{x}'),\end{aligned} \tag{2.5}$$

and use a straight-line path with impact parameter $\boldsymbol{b}$ for the internuclear motion. We further introduce the Fourier representation of the target potential (which is taken to be a purely Coulombic field, $V_T(\boldsymbol{x}) = -(Z_T/2\pi^2)\int(d\boldsymbol{p}/p^2)e^{i\boldsymbol{p}_\perp(\boldsymbol{x}'_\perp + \boldsymbol{b})}e^{ip_z\gamma(z' + vt')}$) such that the

time integrals become trivial. Then the transition amplitude (2.1) turns into

$$a_{fi}^{IA} = \frac{iZ_T}{\pi}\sqrt{\frac{1+\gamma}{2}}\sum_{s=1}^{4}\int d\boldsymbol{q}\int\frac{d\boldsymbol{p}}{p^2}e^{i(\boldsymbol{p}_\perp+\boldsymbol{q}_\perp)\boldsymbol{b}}T_0(s,\boldsymbol{q},\boldsymbol{p}) \times\left[u_q^{(s)+}\left(1-\frac{\gamma v/c}{1+\gamma}\alpha_z\right)\varphi_{i,T}^{(\sigma_i)}(\boldsymbol{q}_0)\right] \times\delta(E_f'+p_z\gamma v+q_z v-E_i^T/\gamma), \quad (2.6)$$

where $\varphi_{i,T}^{(\sigma_i)}(\boldsymbol{q}_0)$ is the initial-state wavefunction in momentum space, and $\boldsymbol{q}_0=(\boldsymbol{q}_\perp,q_{0z})$ with $q_{0z}=E_i^T v/c^2+q_z/\gamma$. T_0 is the transition matrix element,

$$T_0(s,\boldsymbol{q},\boldsymbol{p}) = \int d\boldsymbol{x}'\psi_{f,P}^{(\sigma_f)'+}(\boldsymbol{x}')e^{i\boldsymbol{p}_\perp\boldsymbol{x}'_\perp+ip_z\gamma z'}\left(1+\frac{v}{c}\alpha_z\right)\psi_{q,P}^{(s)'}(\boldsymbol{x}'). \quad (2.7)$$

The doubly differential cross-section for electron emission is obtained by means of integration over impact parameter, as well as averaging and summing, respectively, over the initial and final spin states. Using the Lorentz invariance of the phase space element, $d\boldsymbol{k}_f'/(E_f'/c^2)=d\boldsymbol{k}_f/(E_f/c^2)$, one obtains this cross-section in the laboratory frame,

$$\frac{d^2\sigma^{ECC}}{dE_f d\Omega_f} = \frac{k_f E_f'}{c^2}\frac{1}{2}\sum_{\sigma_i,\sigma_f}\int d^2\boldsymbol{b}\left|a_{fi}^{IA}\right|^2 \quad (2.8)$$

$$= \frac{k_f E_f'}{c^2 v}Z_T^2(1+\gamma)\sum_{\sigma_i,\sigma_f}\int d\boldsymbol{q}'\delta(E_f'+q_z' v-E_i^T/\gamma) \times\left|\sum_{s=1}^{4}\int d\boldsymbol{p}\frac{1}{p^2}T_0(s,\boldsymbol{q},\boldsymbol{p}) \times\left[u_q^{(s)+}\left(1-\frac{\gamma v/c}{1+\gamma}\alpha_z\right)\varphi_{i,T}^{(\sigma_i)}(\boldsymbol{q}_0)\right]\right|^2$$

where E_f and $d\Omega_f$, respectively, are the energy and solid angle of the emitted electron, and $\boldsymbol{q}'$ is related to $\boldsymbol{q}$ by means of $\boldsymbol{q}=(\boldsymbol{q}_\perp'-\boldsymbol{p}_\perp,q_z'-p_z\gamma)$.

For the evaluation of (2.8) semirelativistic Darwin and Sommerfeld-Maue wavefunctions are used, respectively, for the bound and continuum electronic states (see e.g. [20,21]). The Sommerfeld-Maue functions (which are exact up to first order in Z_P/c) have been tested against an exact relativistic (partial-wave) representation in the case of bremsstrahlung [22] and were also used for the radiative capture to continuum [12]. Such wavefunctions allow for a representation of the transition matrix element in closed form. Defining the bound-state and continuum-state normalization factors,

$$N_i^T=\left[1+\left(\frac{Z_T\mu}{n_i}\right)^2\right]^{-\frac{1}{2}},\quad N_q=(2\pi)^{-\frac{3}{2}}e^{\pi\eta_q/2}\Gamma(1-i\eta_q), \qquad \eta_q=\frac{Z_P E_q}{qc^2}, \quad (2.9)$$

where $\mu=c/(E_i^T+c^2)$, $E_q=(q^2c^2+c^4)^{\frac{1}{2}}$, and using completeness for the spin summation one obtains (for s-states)

$$\sum_{s=1}^{4}T_0(s,\boldsymbol{q},\boldsymbol{p})\left[u_q^{(s)+}\left(1-\frac{\gamma v/c}{1+\gamma}\alpha_z\right)\varphi_{i,T}^{(\sigma_i)}(\boldsymbol{q}_0)\right] = N_{k_f'}N_q N_i^T\left[u_{k_f'}^{(\sigma_f)+}I(\boldsymbol{p}',\boldsymbol{q})\left(1-\frac{\gamma v/c}{1+\gamma}\alpha_z\right)a_i^{(\sigma_i)}(\boldsymbol{q}_0)\right] \times\tilde{\varphi}_{i,T}(\boldsymbol{q}_0) \quad (2.10)$$

where $\tilde{\varphi}_{i,T}(\boldsymbol{q}_0)$ is the nonrelativistic bound-state momentum-space function, $a_i^{(\sigma_i)}(\boldsymbol{q}_0)$ the four-spinor of the Darwin function, and

$$I(\boldsymbol{p}',\boldsymbol{q}) = \int d\boldsymbol{x}'\left\{\left(1+\frac{ic}{2E_f'}\boldsymbol{\alpha}\boldsymbol{\nabla}\right){}_1F_1(i\eta_f,1,i(k_f'r'+\boldsymbol{k}_f'\boldsymbol{x}'))\right\} \times e^{i\boldsymbol{p}'\boldsymbol{x}'}\left(1+\frac{v}{c}\alpha_z\right)\left(1-\frac{ic}{2E_q}\boldsymbol{\alpha}\boldsymbol{\nabla}\right) \times{}_1F_1(i\eta_q,1,i(qr'-\boldsymbol{q}\boldsymbol{x}')) \quad (2.11)$$

with $\eta_f=Z_P E_f'/(k_f'c^2)$ and $\boldsymbol{p}'=(\boldsymbol{p}'_\perp,p_z')$ with $\boldsymbol{p}'_\perp=\boldsymbol{p}_\perp+\boldsymbol{q}_\perp-\boldsymbol{k}'_{f\perp}$, $p_z'=\gamma p_z+q_z-k'_{fz}$.

The integrals over the confluent hypergeometric functions ${}_1F_1$ can be carried out analytically with the help of Nordsieck's formula [23], see [12,21].

The remaining multiple integral in (2.8) is done with the help of a transverse peaking approximation which also was applied in the nonrelativistic case [15]. This approximation relies on the fact that $\tilde{\varphi}_{i,T}(\boldsymbol{q}_0)$ is strongly peaked at $q_0=\sqrt{q_\perp^2+q_{0z}^2}=0$. Therefore, the transverse momentum components $\boldsymbol{q}_\perp$ are set equal to zero in all factors of (2.10) multiplying $\tilde{\varphi}_{i,T}(\boldsymbol{q}_0)$. For relativistic collision velocities this approximation is even more justified since a large longitudinal momentum transfer is required in $I(\boldsymbol{p}',\boldsymbol{q})$ to ensure energy conservation. For numerical convenience we introduce $\boldsymbol{p}'$ as integration variable in the transition amplitude in place of $\boldsymbol{p}$ and thus obtain for the differential cross-section

$$\frac{d^2\sigma^{ECC}}{dE_f d\Omega_f} = \frac{k_f E_f'}{c^2 v}\frac{Z_T^2(1+\gamma)}{\gamma^2}\left|N_{k_f'}N_i^T\right|^2 \times\int d\boldsymbol{p}'\delta(E_f'-E_i^T/\gamma+p_z' v+k'_{fz}v)\sum_{\sigma_i,\sigma_f}\left|\int_{-\infty}^{\infty}dq_z N_{|q_z|} \times\left[u_{k_f'}^{(\sigma_f)+}I(\boldsymbol{p}',q_z\boldsymbol{e}_z)\left(1-\frac{\gamma v/c}{1+\gamma}\alpha_z\right)a_i^{(\sigma_i)}(q_{0z}\boldsymbol{e}_z)\right] \times F_0(\boldsymbol{p}',q_z)\right|^2. \quad (2.12)$$

For a $1s$ state, the integral F_0 over the transverse components of $\boldsymbol{q}$ is given by

$$F_0(\boldsymbol{p}', q_z) = \int d\boldsymbol{q}_\perp \frac{1}{(\boldsymbol{p}'_\perp - \boldsymbol{q}_\perp + \boldsymbol{k}'_{f\perp})^2 + \frac{1}{\gamma^2}(p'_z - q_z + k'_{fz})^2} \tilde{\varphi}_{i,T}(\boldsymbol{q}_0)$$
$$= 2\sqrt{2} Z_T^{\frac{5}{2}} \left[\frac{1}{\beta_0} \left(\frac{a^2 + p_\perp^{''2}}{b_0^2} - 1 \right) - \frac{\alpha_0}{2\beta_0^{\frac{3}{2}}} \ln \frac{2\sqrt{\beta_0}(a^2 + p_\perp^{''2}) + 2\beta_0 + \alpha_0 b_0^2}{b_0^2(\alpha_0 + 2\sqrt{\beta_0})} \right] \quad (2.13)$$

with the parameters $\boldsymbol{p}''_\perp = \boldsymbol{p}'_\perp + \boldsymbol{k}'_{f\perp}$ and $a = (p'_z + k'_{fz} - q_z)/\gamma$, $b_0^2 = Z_T^2 + q_{0z}^2$, $\alpha_0 = 2(a^2 - b_0^2 - p_\perp^{''2})$, $\beta_0 = (a^2 + p_\perp^{''2} - b_0^2)^2 + 4b_0^2 p_\perp^{''2}$. We note that the p'_z-integral is performed by means of the δ-function whereas the q_z-integral can be restricted to the interval $[-2\gamma v, -\gamma v/4]$ for moderate γ. The strong singularity at $q_z = (p_\perp^{'2} + p_z^{'2})/2p'_z$ can be handled in the same way as in the nonrelativistic case [15].

2.2 Radiative ionization (RI)

For radiative transitions the interaction in (2.1) arises from the photon field, $\gamma_0 \hat{S} \mathbb{A}(x) \hat{S}^{-1} = -\boldsymbol{\alpha} \boldsymbol{A}'_\lambda e^{ik'x'} d_\lambda^+$ with $\boldsymbol{A}'_\lambda = c\boldsymbol{e}_\lambda/(2\pi\omega'^{1/2})$ where $k' = (\omega'/c, -\boldsymbol{k}')$ is the 4-momentum of the photon and $\boldsymbol{e}_\lambda$ its polarization direction. Therefore, the basic difference to the ECC theory is the occurrence of the radiation matrix element [12]

$$\boldsymbol{W}_{rad}(\sigma_f, s, \boldsymbol{q}) = \int d\boldsymbol{x}' \psi_{f,P}^{(\sigma_f)'+}(\boldsymbol{x}') \boldsymbol{\alpha} e^{-i\boldsymbol{k}'\boldsymbol{x}'} \psi_{q,P}^{(s)'}(\boldsymbol{x}') \quad (2.14)$$

in place of the Coulomb transition matrix element $T_0(s, \boldsymbol{q}, \boldsymbol{p})/p^2$ from (2.7). The fourfold differential cross-section for the emission of an electron with energy E_f into the solid angle $d\Omega_f$ accompanied by the creation of a photon with energy $\omega = kc$ is given by

$$\frac{d^4\sigma^{RI}}{dE_f d\Omega_f d\omega d\Omega} = \frac{k_f \omega \omega' E'_f}{2c^5} \sum_{\lambda, \sigma_i, \sigma_f} \int d^2\boldsymbol{b} \left| \tilde{a}_{fi}^{IA} \right|^2 \quad (2.15)$$

where the sum over λ runs over the two polarization directions of the photon, and $d\Omega$ is the photon solid angle. In the impulse approximation, one has [12]

$$\tilde{a}_{fi}^{IA} = \frac{2\pi i}{\gamma} \sqrt{\frac{1+\gamma}{2}} \boldsymbol{A}'_\lambda \sum_{s=1}^{2} \int d\boldsymbol{q} e^{i\boldsymbol{q}_\perp \boldsymbol{b}} \boldsymbol{W}_{rad}(\sigma_f, s, \boldsymbol{q}) \times \left[u_q^{(s)+} \left(1 - \frac{\gamma v/c}{1+\gamma} \alpha_z \right) \varphi_{i,T}^{(\sigma_i)}(\boldsymbol{q}_0) \right] \times \delta(E'_f + \omega' - E_i^T/\gamma + q_z v) \quad (2.16)$$

with $\boldsymbol{q}_0 = (\boldsymbol{q}_\perp, q_{0z})$ and $q_{0z} = E_i^T v/c^2 + q_z/\gamma$ as above.

In order to compare the resulting electron distribution with the one from the nonradiative capture, the differential cross-section (2.15) has to be integrated over the photon degrees of freedom. For electron emission not parallel to the beam axis, this involves a threefold integral,

$$\frac{d^2\sigma^{RI}}{dE_f d\Omega_f} = 2 \int_0^\pi d\varphi_f \int_0^\pi \sin\theta d\theta \int_{\omega_{min}}^{\omega_{max}} d\omega \frac{d^4\sigma^{RI}}{dE_f d\Omega_f d\omega d\Omega}. \quad (2.17)$$

The angle θ is the polar photon angle and φ_f is the difference between electron and photon azimuthal angles. The energy integral can be confined to a small interval around the peak frequency $\omega_{peak} = (E_i^T - E_f + vk_f \cos\vartheta_f)/(1 - (v/c)\cos\theta)$ of half-width $\sim 3(Z_T/n_i)v/(1 - (v/c)\cos\theta)$ which is attributed to the target Compton profile.

3 Results

Calculations have been performed for fast projectiles ranging from helium to uranium and for targets ranging from hydrogen to argon under the restriction $Z_P \geq 2Z_T$. For targets different from H, Slater-screened hydrogenic wavefunctions and experimental binding energies are used for the initial states. The target field entering into the ECC cross-section is taken Coulombic to the same effective charge. The neglect of the outer-shell screening in V_T is justified for the high collision velocities which are considered here: the resulting high momenta of the intermediate states (being of the order of v) combined with the near-zero final-state momenta require large momentum transfers and hence close collisions. The only case of a projectile carrying electrons, U^{88+}, is treated in terms of a bare projectile with $Z_P = 88$, the full screening by the tightly bound electrons being a reasonable approximation for the continuum states.

3.1 Electron spectra

In order to give an overview, we start by showing the global energy dependence of the electrons from the ECC and RI processes emitted into the forward direction. Figure 1 shows the electron spectra from 30 MeV/amu Ar^{18+} + H collisions at an emission angle of 1.5° (which may be identified with a suitable detector resolution and turns the 0° cusp into a finite forward peak). For such energetic collisions ($v = 33.85$ a.u.), RI is largely dominating over ECC in the forward peak region. It also provides a much sharper peak (which in contrast to ECC is skewed to the *high-energy* side and is therefore located *above* the cusp position $E_{cusp,kin} = 16.34$ keV). At energies beyond 50 keV the binary encounter peak emerges in the electron spectra. There, as well as for the soft electrons, the relative importance of the RI and ECC processes is reversed. It should be noted, however, that for electron energies tending to zero, the impulse approximation as presented above is no longer an adequate theory because then the target

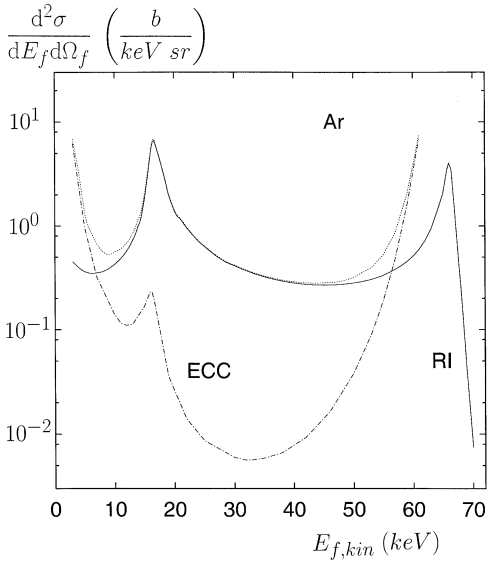

Fig. 1. Doubly differential cross-section for electron emission at $\vartheta_f = 1.5°$ in 30 MeV/amu Ar^{18+} + H collisions as a function of kinetic electron energy. Shown is the contribution from nonradiative electron capture to continuum (chain curve), from radiative ionization (full curve) and their sum (dotted curve).

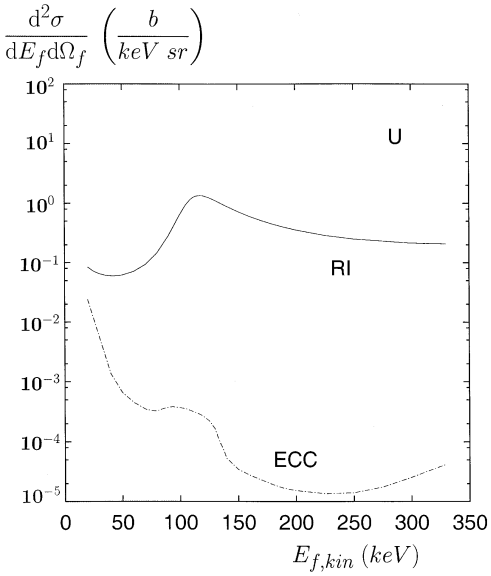

Fig. 2. Doubly differential cross-section for electron emission at $\vartheta_f = 5°$ in 200 MeV/amu U^{92+} + H collisions; (———) radiative ionization, (− · − · −) nonradiative electron capture to continuum (smoothed in the forward peak region).

potential cannot be neglected in the final-state electronic wavefunction.

In Figure 2 the electron spectra from 200 MeV/amu U^{92+} + H collisions are displayed for an emission angle of 5°. At the relativistic velocity of $v = 77.6$, the RI mechanism is much more important than ECC in the whole energy region considered. While the forward ECC peak has shrinked to a mere shoulder at this larger angle, RI still shows a pronounced peak. We note that the RI calculations can be performed with high accuracy (∼1 percent (except at the binary encounter peak maximum), independent of the collision system), whereas one has severe convergence problems for ECC caused by the strongly singular and rapidly oscillating integrand $I(\boldsymbol{p}', \boldsymbol{q})$ if the Sommerfeld parameters η_f and η_q are very large (i.e. high Z_P/k'_f and Z_P/v). For the ECC of Figure 2 the accuracy is estimated ∼5 percent far away from the cusp, deteriorating to ∼25 percent in the cusp region.

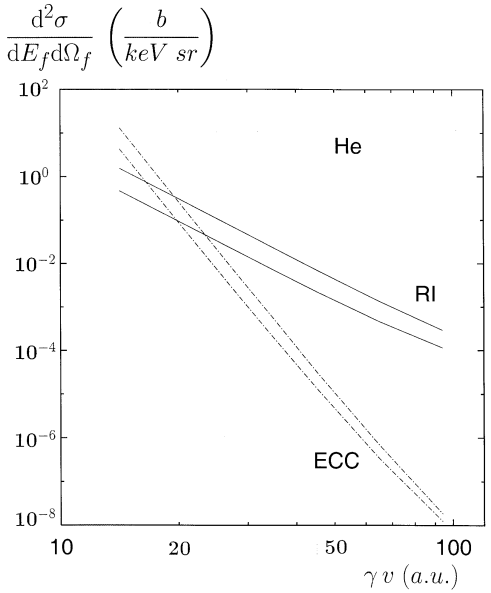

Fig. 3. Doubly differential cross-section in the RI forward peak maximum from He^{2+} + H collisions as a function of impact momentum γv; (———) radiative ionization, (− · − · −) nonradiative electron capture to continuum. Upper and lower curves, respectively, correspond to electron emission angles of $\vartheta_f = 1.5°$ and 5°.

3.2 Scaling laws and the RI/ECC crossing velocity

Let us compare ECC and RI in the cusp region, i.e. for kinetic electron energies near zero in the projectile rest frame. More precisely, we consider the doubly differential cross-sections (2.12) and (2.17) for a fixed forward emission angle at the maximum E^{RI}_{peak} of the RI peak. The location of this maximum as well as the corresponding intensities depend on the collision velocity v and on the projectile charge Z_P. To begin with, we restrict ourselves to bare projectiles and to a hydrogen target.

Figure 3 depicts the ECC and RI cross-sections at E^{RI}_{peak} for He^{2+} + H as a function of γv for two forward angles, $\vartheta_f = 1.5°$ and 5°. It is seen that for fixed ϑ_f the curves cross at $\gamma v \approx 20$ (corresponding to a collision energy of 10 MeV/amu) and that the ECC and RI curves, respectively, are nearly parallel for the two angles. We have carried out similar calculations for Ar, Kr and Xe projectiles and have found that the crossing velocity hardly depends on Z_P ($\gamma v_{cr} = 19.8$ for He, 21.1 for Ar, 21.3 for Kr and 22.0 for Xe at $\vartheta_f = 5°$). In order to compare

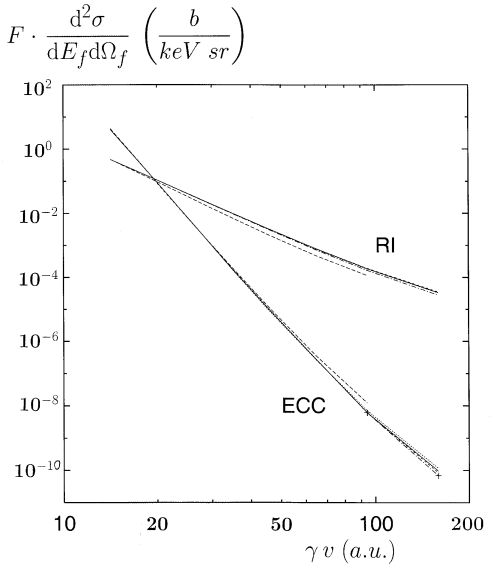

Fig. 4. Scaled doubly differential cross-section in the RI forward peak maximum at $\vartheta_f = 5°$ for bare projectiles colliding with H as a function of γv. The curves labeled RI correspond to radiative ionization and are, by a suitably chosen factor F, normalized to the He^{2+} + H result at $v = 14.1$ a.u. The curves labeled ECC correspond to nonradiative capture to continuum and are normalized to the helium result at $v = 27.86$, except for uranium (marked by +) which is normalized to the Ar^{18+} + H result at $v = 77.6$. The projectiles are He^{2+} (– – – –), Ar^{18+} (———), Kr^{36+} (- - - - -), Xe^{54+} (· · · · ·), and U^{92+} (– · – · –).

the velocity dependence of the peak cross-sections, we have normalized in Figure 4 the cross-sections for various projectiles to the respective cross-section for He at a fixed collision velocity (except for U where, for convergence reasons, the lowest velocity considered is $v = 77.6$ where a normalization to He, already distinct from the bulk, is not meaningful). For RI as well as for ECC, these scaled cross-sections tend to form a common line, with some spread at the highest velocities considered. Only for the lightest projectile, He, the results are slightly above (for ECC) respectively below (for RI) the bulk. At the lower velocities, the line is approximately straight, indicating a power-law dependence. For Ar for example, the RI peak cross-section behaves like $(\gamma v)^{-n}$ with n decreasing from 4.3 (near $v = 15$) to 3.3 (near $v = 100$).

An immediate consequence of this scaling property, combined with the approximate constancy of v_{cr}, is a common (for both ECC and RI) dependence on the projectile charge, irrespective of the collision velocity. Figure 5a shows that the RI peak cross-sections (at fixed velocity) scale with Z_P according to Z_P^m with $m \sim 2.3$, except for He. In Figure 5b, the Z_P-dependence of the ECC cross-sections is displayed. Except for uranium, the power is close to the one for RI, with a minor velocity dependence ($m \sim 2.6$ for the lowest v, decreasing to $m \sim 2.4$ at high v). This slightly steeper increase for ECC (together with the stronger decrease of ECC with γv) causes the marginal increase of γv_{cr} with Z_P.

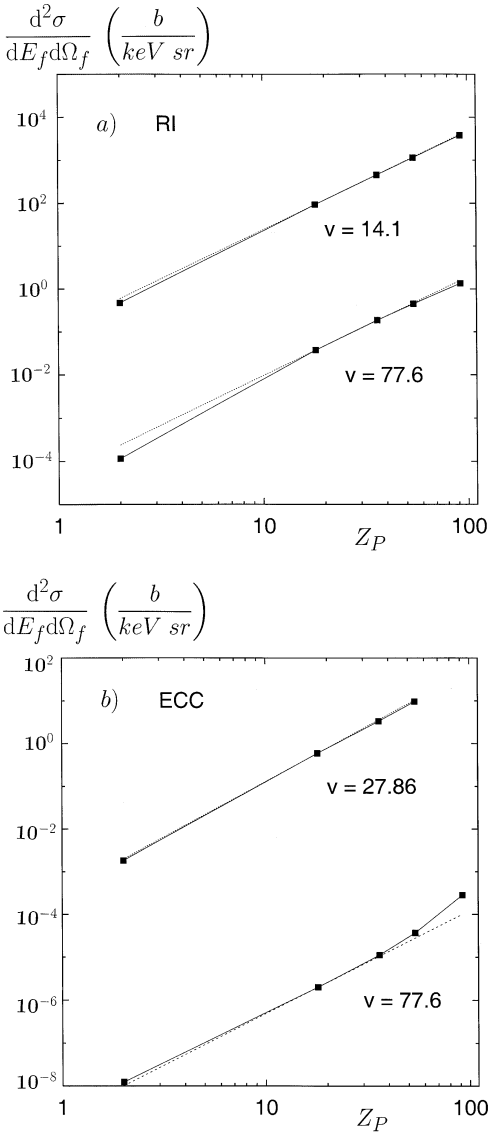

Fig. 5. Projectile charge dependence of the doubly differential cross-section in the RI forward peak maximum for a hydrogen target at fixed collision velocity and $\vartheta_f = 5°$. (a) Radiative ionization (■) at $v = 14.1$ (top) and 77.6 (bottom). The dotted straight lines display Z_P^m with $m = 2.3$ (normalized at $Z_P = 18$) for comparison. (b) Nonradiative capture to continuum (■) at $v = 27.86$ (top) and 77.6 (bottom). The straight lines display Z_P^m with $m = 2.6$ (· · · · ·) and $m = 2.4$ (– – – –). The full curves are eye-guides.

Let us now consider heavier targets, and let us restrict ourselves to capture from the K-shell. Figure 6 displays the forward peak cross-sections for Ar and Xe projectiles colliding with H, He and N targets. One observes that the RI peak cross-sections do not depend on the target species. This is an immediate consequence of the normalization of the bound-state wavefunction, since the integrations which are necessary to evaluate the doubly differential RI cross-section involve a (three-dimensional) integral over the bound-state momentum-space function. For the ECC peak cross-sections on the other hand, there is a

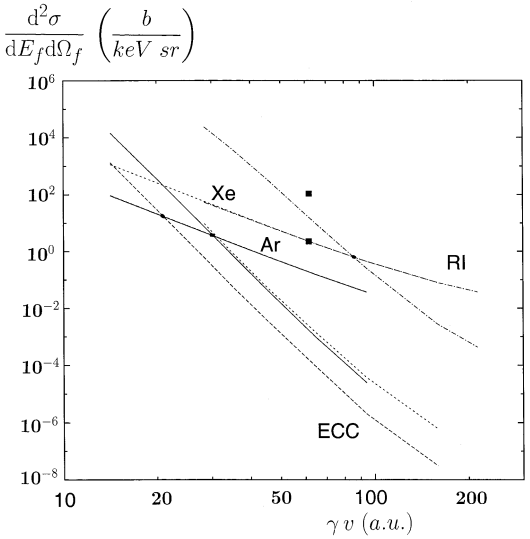

Fig. 6. Doubly differential K-shell capture cross-section (per electron) in the RI forward peak maximum at $\vartheta_f = 5°$ for Ar^{18+} and Xe^{54+} colliding with various targets as a function of γv. The bunch of steep curves result from nonradiative capture to continuum, the flat curves originate from radiative ionization: Ar^{18+} + H (− − − −), Ar^{18+} + He (——), Xe^{54+} + H (- - - - -) and Xe^{54+} + N (− · − · −). The black dots mark the crossing velocity for the three targets. The symbols (■) are experimental results [3,24] for nitrogen K-shell capture by U^{88+} as described in the text.

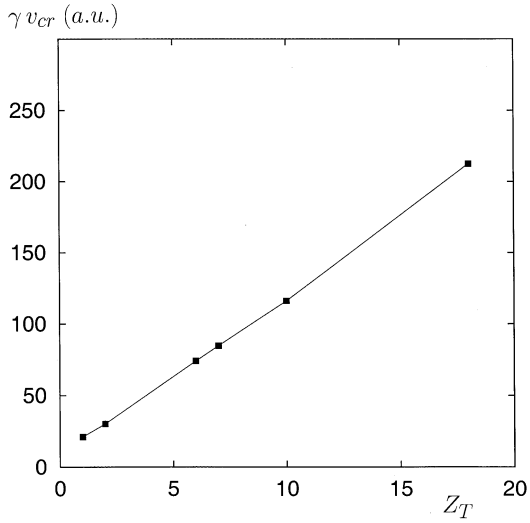

Fig. 7. Crossing velocity (multiplied by γ) as a function of target charge Z_T for K-shell ionization by Xe^{54+} projectiles ($\vartheta_f = 5°$). The black squares are the calculated values and the full line is an eye-guide.

strong increase with Z_T, which again hardly depends on the collision velocity (as is obvious from the nearly parallel lines for Xe^{54+} + H and Ar^{18+} + He combined with the results from Fig. 4). In part, this increase with Z_T is caused by the extra appearance of V_T in the transition amplitude. However, due to an additional maximum in the momentum integral in (2.12) (apart from the one near $q_{0z} = 0$) which is attributed to the singularity of the Coulomb field, higher momenta in the bound-state wavefunction come into play. These are strongly enhanced for more tightly bound electrons.

In order to compare with experimental cusp results on U^{88+}+N_2 at $v = 56.24$ a.u., we have estimated the ECC yield from the target L-shell to be about 4.3 percent (per electron) of the K-shell capture yield at this collision velocity. Therefore we approximate $d^2\sigma_{exp}^{ECC} = 2(2d^2\sigma_{exp}^{ECC}(1s) + 2d^2\sigma_{exp}^{ECC}(2s) + 3d^2\sigma_{exp}^{ECC}(2p)) \approx 2 \times 2.22 d^2\sigma_{exp}^{ECC}(1s)$, in contrast to RI where all electrons give the same contribution, $d^2\sigma_{exp}^{RI} \approx 2\times 7 d^2\sigma_{exp}^{RI}(1s)$. The prefactor 2 accounts for the N_2 molecule. Since the experimental yields are so far only relative, we have normalized $d^2\sigma_{exp}^{RI}(1s)$ to the calculated RI yield for Xe + N. (In order to verify the scaling property we have calculated the forward-peak RI and ECC cross-sections for U ($Z_P = 88$) + N and have found that, if RI is normalized to the Xe + N yield, the corresponding ECC yield falls on top of the Xe + N yield within 5 percent.) As shown in Figure 6, experiment confirms that the nitrogen crossing velocity is well above those for H and He targets. The underestimation of the experimental ECC yield by theory is partly ascribed to the semirelativistic wavefunctions which do not have sufficiently large high-momentum tails. On the other hand, the experimental ECC yield is not measured directly, but obtained by subtracting the simultaneously measured RI and one-electron loss yields from the total electron yield [24]. So it may include contributions from other processes (like double electron loss).

The constancy of RI and the increase of K-shell ECC with target nuclear charge induce a monotonous rise of the crossing velocity with Z_T. This is shown in Figure 7 for Xe projectiles colliding with targets up to Ar (for Xe^{54+} + Ar, $Z_T/Z_P = 18/54 \approx 0.33$ and $Z_T/v_{cr} = 18/115 \approx 0.16$ such that the impulse approximation should still give reliable results). It is seen that the increase of v_{cr} with Z_T is somewhat less than linear.

4 Conclusion

We have calculated and analyzed the two mechanisms which contribute to continuum electron capture during fast collisions of bare, heavy projectiles with light targets. Particular interest was devoted to the dependence of the doubly differential cross-sections for electron emission on collision velocity, projectile charge and target species.

For the study of the relative importance of the two capture mechanisms we have selected the forward peak maximum at near-zero emission angles. This maximum results from electrons captured into low-lying projectile continuum eigenstates. Its precise position indicates the shift of the forward peak (downwards for ECC and upwards for RI, relative to the cusp position) inherent in a higher-order theory. For high but still nonrelativistic collision energies we have verified the common scaling of both capture

mechanisms with projectile charge, although the increase with Z_P is substantially weaker than the Z_P^3-Born result (for RI and ECC we find $Z_P^{2.3}$ and $Z_P^{2.6}$, respectively).

When advancing to higher collision velocities (but still in the weak-relativistic regime, $\gamma \lesssim 2$) the scaling with projectile charge is fairly well maintained and leads to a velocity dependence of RI, respectively ECC, which is nearly independent of the projectile and the target species. However, this v-dependence does not follow any power law, but gets gradually weaker as v increases. For ECC for example, if expressed in terms of $(\gamma v)^{-n}$, $n \sim 11$ for $v \lesssim 35$, $n \sim 8$ near $v = 90$ and $n \sim 5.5$ near $v = 120$. Note that within our numerical approach it does not seem reasonable (particularly not for ECC) to go beyond the weak-relativistic regime and to much heavier targets. This would require a more accurate representation of the atomic wavefunctions which takes proper account of the relativistic high-momentum tails.

As a consequence of the common scaling with Z_P, the RI/ECC crossing velocity is indeed to a good approximation independent of the projectile, being $v_{cr} \sim 21$ a.u. for a hydrogen target. A similar crossing velocity is also expected for the capture of valence electrons from heavier targets. Turning to inner-shell capture from heavier targets, it was found that radiative ionization does not depend on the target species whereas ECC shows a rapid increase with the target nuclear charge. When proceeding from He to C, Ne and Ar targets, v_{cr} for K-shell capture is predicted to increase from $v_{cr} \sim 29.5$ to 65, 88.5 and 115 a.u., respectively. Thus for the heavier targets, a relativistic formulation of the theory is important, as the onset of relativistic effects (beyond the shift of the peak position) occurs already at $v = 30$–50, depending on the projectile and on the capture mechanism. Pilot experiments have verified that at $v = 56$ a.u., ECC is still largely dominating over RI if the target is nitrogen.

Finally, we remark that the relative importance of RI and ECC varies considerably over the electron spectrum. Since ECC strongly increases for low-energy electrons as well as for electrons near the binary encounter peak, it may well dominate the spectrum at these locations even in cases where RI has a much higher intensity in the forward peak region. However, a detailed investigation is beyond of the scope of the present work.

I would like to thank S. Hagmann for stimulating this work and for many fruitful discussions. I also wish to express my gratitude to J.M. Rost and to the GSI Darmstadt for supporting contacts with the physical community.

References

1. R. Dörner, V. Mergel, O. Jagutzki, L. Spielberger, J. Ullrich, R. Moshammer, H. Schmidt-Böcking, Phys. Rep. **330**, 95 (2000)
2. M. Nofal et al., AMOP Spring Meeting, Verhandl. DPG (IV) **41**, 7/33 (2006)
3. M. Nofal et al., GSI Scientific Annual Report, 2005
4. J.S. Briggs, K. Dettmann, Phys. Rev. Lett. **33**, 1123 (1974)
5. M.E. Rudd, J. Macek, *Case Studies in Atomic Physics* (North Holland, Amsterdam, 1972), Vol. 3, p. 48
6. R. Shakeshaft, L. Spruch, J. Phys. B **11**, L621 (1978)
7. M.W. Lucas, W. Steckelmacher, J. Macek, J.E. Potter, J. Phys. B **13**, 4833 (1980)
8. M.L. Martiarena, C.R. Garibotti, Phys. Lett. A **113**, 307 (1985)
9. D.H. Jakubaßa-Amundsen, J. Phys. B **20**, 325 (1987)
10. D.H. Jakubaßa, M. Kleber, Z. Phys. A **273**, 29 (1975)
11. A. Yamadera, K. Ishii, K. Sera, M. Sebata, S. Morita, Phys. Rev. A **23**, 24 (1981)
12. D.H. Jakubaßa-Amundsen, J. Phys. B **36**, 1971 (2003)
13. T. Ludziejewski et al., J. Phys. B **31**, 2601 (1998)
14. D.H. Jakubaßa-Amundsen, Rad. Phys. Chem. (in print, 2006)
15. D.H. Jakubaßa-Amundsen, J. Phys. B **16**, 1767 (1983)
16. D.H. Jakubaßa-Amundsen, *Lecture Notes in Physics*, edited by K.O. Groeneveld, W. Meckbach, I.A. Sellin (Springer, Berlin, 1984), Vol. 213, p. 17
17. D.H. Jakubaßa-Amundsen, Phys. Rev. A **38**, 70 (1988)
18. D. Bjorken, S.D. Drell, *Relativistic Quantum Mechanics* (BI, Mannheim, 1964)
19. E.M. Rose, *Relativistic Electron Theory* (BI, Mannheim, 1971), Vol. 1, Sect. III
20. D.M. Davidović, B.L. Moiseiwitsch, P.H. Norrington, J. Phys. B **11**, 847 (1978)
21. G. Elwert, E. Haug, Phys. Rev. **183**, 90 (1969)
22. C.D. Shaffer, X.-M. Tong, R.H. Pratt, Phys. Rev. A **53**, 4158 (1996)
23. A. Nordsieck, Phys. Rev. **93**, 785 (1954)
24. S. Hagmann, private communication; M. Nofal et al., preprint (2006)